HHS Public Access

Author manuscript

Science. Author manuscript; available in PMC 2021 June 25.

Published in final edited form as:

Science. 2020 October 23; 370(6515): 431–436. doi:10.1126/science.abb4608.

Orderly Compartmental Mapping of Premotor Inhibitory Inputs in Developing Spinal Cord

Sandeep Kishore[1], **Eli Cadoff**[1], **Moneeza Agha**[1], **David L. McLean**[1,*]

[1]Department of Neurobiology, Northwestern University, Evanston, Illinois 60208, USA.

Abstract

In vertebrates, movements of increasing speed involve the orderly recruitment of different types of spinal motor neurons. However, it is not known how premotor inhibitory circuits are organized to ensure alternating patterns of antagonistic motor output at different speeds. Here, we find that distinct types of commissural inhibitory interneurons in zebrafish form compartmental microcircuits during development that align the potency of reciprocal inhibition with recruitment order. Axonal microcircuits develop first and provide the most potent inhibition of antagonistic motor neurons during the fastest movements, followed by perisomatic microcircuits, and then dendritic microcircuits that provide the weakest inhibition during the slowest movements. This pattern bridges motor neuron types, although faster, earlier-born motor neurons exhibit stronger perisomatic innervation. The conversion of a temporal sequence of neuronal development into a spatial pattern of reciprocal inhibitory connections provides an ‘ontogenotopic’ solution to the problem of shaping spinal motor output at different speeds of movement.

One Sentence Summary:

Developing spinal inhibitory interneurons form compartmental microcircuits that ensure appropriate patterns of motor output later on in life.

Like ancestral vertebrates, zebrafish move through the water using axial muscle contractions that alternate from left to right across the body (1). To move more quickly, larger motor neurons born during a ‘primary’ wave of neurogenesis are recruited into an active pool that includes more numerous smaller motor neurons born during a ‘secondary’ wave of neurogenesis that are also recruited at slower speeds (2, 3). By free-swimming larval and adult stages, the sequential development of spinal motor neurons has formed a topographic map of recruitment from ventral to dorsal during increases in body bending frequency and thus the speed of locomotion (4, 5). Reciprocal left-right alternation during swimming is maintained by glycinergic commissural inhibitory interneurons 6, 7), which are also topographically organized based on recruitment order in zebrafish (4). However, it is not clear how commissural inhibitory circuits are assembled or organized to ensure left-right

*Correspondence to: david-mclean@northwestern.edu.

Author contributions: Conceptualization, S.K., D.M.; Methodology, S.K., D.M.; Validation, D.M.; Formal analysis, S.K., D.M.; Investigation, S.K, E.C, M.A.; Writing, S.K., D.M.; Visualization, S.K., D.M.; Supervision, D.M.

Competing interests: Authors declare no competing interests.

Data and materials availability: All data not presented in the main text or the supplementary materials are freely available upon reasonable request.

alternation in a larger target population comprised of bigger neurons at higher speeds, given the challenge in linking synaptic connectivity to neuronal identity and recruitment order.

Larger motor neurons receive stronger perisomatic glycinergic inhibition

To begin assessing the speed-dependent organization of premotor inhibitory inputs, we first asked whether differences exist in the compartmental distribution of inhibitory synapses among motor neurons recruited at different speeds. We injected Gal4-UAS constructs (see Methods) in 1–2 cell stage embryos to sparsely label individual primary (n = 15) and secondary (n = 24) motor neurons with fluorescent reporters (Fig. 1A,B). We focused on glycinergic synapse distribution using GlyRα1 fused with enhanced GFP (8). In 4–5 day old larvae, this in vivo labeling approach revealed punctate fluorescent signals in the axonic, somatic and dendritic compartments of both types of motor neurons (Fig. 1C). The largest total number of putative inhibitory synapses were observed in the dendrites for both primaries and secondaries (Fig. 1D). However, consistent with the idea that larger motor neurons require more potent perisomatic inhibition to curtail their activity (9), primaries exhibited higher total numbers of putative inhibitory contacts in both somatic and axonic compartments than secondaries (Fig. 1D). From the transverse perspective, GlyRα1 puncta decorated the lateral surface of both primary and secondary motor neurons (Fig. 1F), with putative axonic and somatic synapses concentrated more medially than dendritic synapses (Fig. 1G).

Inhibitory interneurons target different motor neuron compartments

Next, to assess the contribution of commissural inhibitory inputs to GlyRα1 puncta distributions, we focused on dmrt3a-labeled dI6 neurons, which provide a conserved source of commissural inhibition during locomotion (10). We first optimized the GRASP (GFP Reconstitution Across Synaptic Partners) approach for use in zebrafish, which relies on the apposition of pre- and post-synaptic membranes at synapses to reconstitute a split GFP molecule (11, 12). Using Gal4-UAS based approaches (see Methods), we created a transgenic line with all dI6 neurons labeled with pTagRFP and one half of a split GFP molecule tethered to the membrane, as well as all motor neurons with mCerulean and the other half of a split GFP molecule (Fig 2A). The resulting transgenic larvae should have functional GFP at locations where dI6 and motor neurons form connections. This approach revealed GFP puncta medially and laterally, but with a perisomatic bias (Fig. 2B). Consistent with the reconstitution of GFP at synapses, we observed punctate signals at locations where the axons of dI6 interneurons overlapped with the axons, somata and dendrites of unidentified motor neurons (Fig. 2C). To better link inputs in different compartments to different motor neuron types, we sparsely labeled dI6 neurons and motor neurons (n = 12), which confirmed the presence of axonic, somatic and dendritic GFP signals in both primaries and secondaries (Fig. 2D).

Axonic, somatic and dendritic inputs to motor neurons could arise from the same neuron or different neurons. To assess how individual dI6 interneurons contributed to compartmentalization, we used a Gal4-UAS approach to sparsely label dI6 neurons with different cytosolic and synaptophysin-tagged fluorescent proteins in a transgenic line that

labels motor neurons (Fig. 2E,F). dI6 neurons could be divided into discrete types based on their morphologies and distribution of synaptic outputs relative to motor neurons. The first type had large caliber, primarily descending and local axons with synaptophysin puncta concentrated ventrally and medially in close proximity to motor neuron axons (Fig. 2G,H). These neurons are likely commissural local (CoLo) neurons that provide left-right direction control during fast startle responses in larval and adult fish (13–15). Two other types of dI6 interneurons with symmetrically bifurcating axons could be divided into groups with either medial synaptic output close to motor neuron somata or lateral synaptic output concentrated in the dendritic neuropil (Fig. 2G,H). These neurons are likely commissural bifurcating longitudinal (CoBL) neurons, which participate in swimming in larval fish (4, 16). Despite differences in subcellular targeting and axon trajectories, we found no significant difference in the density of synaptophysin puncta related to type, with each averaging 1–2 synapses every 10 microns of axon (Fig. 2I).

Sequential development of dI6 neurons and motor neuron compartments

Given the topographic pattern of CoBL recruitment (4) and the links between birth order and recruitment order in motor neurons (2, 3), we next asked whether dI6 neuron types are also distinguished by sequence of development. We created a transgenic line that enabled in vivo birth-dating using the photoconvertible protein, Dendra (17), which changes from green to red in ultraviolet light. Photoconversions performed on day 1 with imaging performed on day 2 (n = 5; Fig. 3A) revealed a ‘primary’ wave of dI6 neurons that included large caliber, axonic dI6-CoLo neurons (Fig. 3B) and a ‘secondary’ wave of unconverted cells numbering ~10 of 20 per segment (Fig. 3C). To see if dI6 neurons continue to differentiate into free-swimming stages, we performed photoconversions at day 2 and imaging at day 5 (n = 6; Fig. 3D), which revealed a further 20 dI6 neurons added per segment (Fig. 3C). Between day 2 and 5, motor neuron neurogenesis is largely completed (3), but dendrites elaborate extensively (18), suggesting that new territories, if not new neurons, are available for innervation by later developing dI6-CoBLs. Consistent with this idea, there were significant increases in both dI6 neuropil and motor neuron neuropil widths between day 2 and 5 (Fig. 3E,F). Critically, contour density analysis of soma positions also revealed that later developing dI6-CoBLs occupy a more dorsal and medial location in spinal cord (Fig. 3D,G), consistent with the reported recruitment order of CoBLs from dorsal to ventral (4).

dI6 neuron structure and birth order matches recruitment order and veto power

Our observations thus far suggest that distinct types of dI6 neurons emerge in a developmental sequence linking recruitment order and potency of inhibition. To test this idea more directly, we performed electrophysiological recordings from dI6 neurons in current-clamp to monitor their spiking activity while simultaneously recording from primary motor neurons on the opposite side of the body in voltage-clamp to monitor outward inhibitory currents (Fig. 4A,B). dI6 neurons were targeted in transgenic lines based on their dorso-ventral soma positions and morphologies were confirmed after the recording either using epifluorescence illumination (n = 49) or confocal microscopy (n = 12). In a subset of

experiments we also performed photo-conversion on day 2 in transgenic fish to further confirm old versus new dI6 neurons for recordings on day 5 (n = 11). Primary motor neurons were targeted with differential interference contrast imaging based on size and soma location and their identity confirmed by post-hoc epifluorescent images (Fig. 4A).

We first assessed differences in recruitment during 'fictive' escape responses evoked by a brief electrical stimulus to the tail (19). Like real escapes, fictive escapes involve an initial burst of unilateral motor activity that would rapidly turn the fish away, followed by bilateral rhythmic swimming activity to propel the fish forward, which declines in frequency and speed with time (19). As predicted (13–15), axon targeting, early born dI6-CoLos were recruited exclusively during the initial response to the stimulus (Fig. 4B), with firing immediately preceding the short-latency contralateral inhibition that prevents bilateral co-contraction during escape turns (Fig. 4C). dI6-CoBLs were categorized by two types of response. 'Faster' dI6-CoBLs were recruited coincident with or just after dI6-CoLos and continued to fire during the period of strong inhibitory drive to contralateral primary motor neurons (Fig. 4B,C), which is characterized by higher frequency swimming (Fig. 4D). These neurons were also early born and had contralateral axons concentrated perisomatically (Fig. 4C,E). 'Slower' dI6 CoBLs were never recruited during the initial escape (Fig. 4B) and fired more reliably during later periods of weak inhibitory drive to contralateral primaries (Fig. 4B,C) which is characterized by lower frequency swimming (Fig. 4D). These neurons were born after day 2 and had contralateral axons concentrated dendritically (Fig. 4C,E). To assess potential differences in the physiological strength of connectivity, we evoked single spikes in the different types of dI6 neurons and measured inhibitory post-synaptic currents in primary motor neurons (Fig. 4F). Strikingly, differences in subcellular distribution were also matched by differences in the amplitude, failure rate and overall probability of finding a connection (Fig. 4G–I). These observations suggest that differences in veto power conferred by the subcellular distribution of inhibitory inputs (and proximity to the spike initiation zone) are also matched by the amplitude of individual inputs and the number of converging ones.

Discussion

Collectively, our findings provide a developmental solution to the problem of maintaining left-right alternation at different speeds in the spinal cord. Axonic dI6 neurons develop first and have the most potent veto on motor neuron spiking activity as required for left-right direction control during the fastest escape turns, followed by perisomatic dI6 neurons responsible for left-right alternation during higher frequency swimming, and then dendritic dI6 neurons responsible for left-right alternation at lower swimming frequencies (Fig. 4J). This pattern is observed across motor neuron types and ensures they receive appropriate amounts of inhibition at different speeds of movement. Since dendrite-targeting dI6 interneurons are not active during escape bends or at higher frequencies, innervation of secondary motor neurons by axonic and perisomatic dI6 interneurons is critical to maintain left-right alternation at faster speeds (2). Dendritic dI6 innervation of motor neurons likely provides more sparse and selective inhibition of excitatory inputs to provide finer control of motor output at lower speeds (20–22). While our focus was on the dI6 population, a similar

pattern among other cardinal classes of spinal interneurons could help explain the remarkable level of diversity reported from single progenitor domains (23).

The pattern we reveal here resembles the organization of local inhibitory circuits in cortex and hippocampus, where developmentally distinct arrays of GABAergic interneurons targeting different compartments of pyramidal neurons have differential effects on oscillatory activity (24–26). Our findings suggest functionally compartmentalized inhibition has spinal origins and that efforts to decode the functional logic of spinal circuits based on gene expression patterns, positioning, and time of development (27–29) will be helped by considering with whom *and* where neurons form connections. The wiring pattern we demonstrate here suggests that distinct reciprocal inhibitory circuits that arise from a common progenitor pool assemble sequentially following a simple opportunistic rule – form synapses with whatever neuron or neuronal compartment is available when making connections. This 'ontogenotopic' mechanism could complement molecular and spatial cues to dictate the functional assembly of neuronal circuitry more broadly (30).

Supplementary Material

Refer to Web version on PubMed Central for supplementary material.

Acknowledgments:

We thank Elissa Szuter and Rachel Gocker for fish care. We also thank Andrew Miri, Marco Gallio, Cindy Chiu and Michael Jay for feedback on the manuscript.

Funding:

Financial support provided by NIH R01 NS067299 and U19 NS104653.

References and Notes:

1. Fetcho JR, The spinal motor system in early vertebrates and some of its evolutionary changes. Brain Behav Evol 40, 82–97 (1992). [PubMed: 1422809]
2. Kishore xS., Bagnall MW, McLean DL, Systematic shifts in the balance of excitation and inhibition coordinate the activity of axial motor pools at different speeds of locomotion. J Neurosci 34, 14046–14054 (2014). PMC4198544. [PubMed: 25319701]
3. Myers PZ, Eisen JS, Westerfield M, Development and axonal outgrowth of identified motoneurons in the zebrafish. J Neurosci 6, 2278–2289 (1986). PMC6568750. [PubMed: 3746410]
4. McLean DL, Fan J, Higashijima S, Hale ME, Fetcho JR, A topographic map of recruitment in spinal cord. Nature 446, 71–75 (2007). [PubMed: 17330042]
5. Gabriel JP et al., Principles governing recruitment of motoneurons during swimming in zebrafish. Nat Neurosci 14, 93–99 (2011). [PubMed: 21113162]
6. Dale N, Ottersen OP, Roberts A, Storm-Mathisen J, Inhibitory neurones of a motor pattern generator in Xenopus revealed by antibodies to glycine. Nature 324, 255–257 (1986). [PubMed: 3785396]
7. Buchanan JT, Identification of interneurons with contralateral, caudal axons in the lamprey spinal cord: synaptic interactions and morphology. J Neurophysiol 47, 961–975 (1982). [PubMed: 6177842]
8. Chow DM, Zuchowski KA, Fetcho JR, In vivo measurement of glycine receptor turnover and synaptic size reveals differences between functional classes of motoneurons in zebrafish. Curr Biol 27, 1173–1183 (2017). PMC5437745. [PubMed: 28416115]
9. Luscher HR, Ruenzel P, Henneman E, How the size of motoneurones determines their susceptibility to discharge. Nature 282, 859–861 (1979). [PubMed: 229426]

10. Andersson LS et al., Mutations in DMRT3 affect locomotion in horses and spinal circuit function in mice. Nature 488, 642–646 (2012). PMC3523687. [PubMed: 22932389]
11. Feinberg EH et al., GFP Reconstitution Across Synaptic Partners (GRASP) defines cell contacts and synapses in living nervous systems. Neuron 57, 353–363 (2008). [PubMed: 18255029]
12. Macpherson LJ et al., Dynamic labelling of neural connections in multiple colours by trans-synaptic fluorescence complementation. Nat Commun 6, 10024 (2015). PMC4686661. [PubMed: 26635273]
13. Satou C et al., Functional role of a specialized class of spinal commissural inhibitory neurons during fast escapes in zebrafish. J Neurosci 29, 6780–6793 (2009). PMC6665578. [PubMed: 19474306]
14. Liao JC, Fetcho JR, Shared versus specialized glycinergic spinal interneurons in axial motor circuits of larval zebrafish. J Neurosci 28, 12982–12992 (2008). PMC2677998. [PubMed: 19036991]
15. Fetcho JR, Faber DS, Identification of motoneurons and interneurons in the spinal network for escapes initiated by the mauthner cell in goldfish. J Neurosci 8, 4192–4213 (1988). PMC6569477. [PubMed: 3183720]
16. Hale ME, Ritter DA, Fetcho JR, A confocal study of spinal interneurons in living larval zebrafish. J Comp Neurol 437, 1–16 (2001). [PubMed: 11477593]
17. Gurskaya NG et al., Engineering of a monomeric green-to-red photoactivatable fluorescent protein induced by blue light. Nat Biotechnol 24, 461–465 (2006). [PubMed: 16550175]
18. Kishore S, Fetcho JR, Homeostatic regulation of dendritic dynamics in a motor map in vivo. Nat Commun 4, 2086 (2013). PMC3702161. [PubMed: 23803587]
19. McLean DL, Masino MA, Koh IY, Lindquist WB, Fetcho JR, Continuous shifts in the active set of spinal interneurons during changes in locomotor speed. Nat Neurosci 11, 1419–1429 (2008). PMC2735137. [PubMed: 18997790]
20. Fyffe RE, Spatial distribution of recurrent inhibitory synapses on spinal motoneurons in the cat. J Neurophysiol 65, 1134–1149 (1991). [PubMed: 1869909]
21. Edwards DH, Heitler WJ, Krasne FB, Fifty years of a command neuron: the neurobiology of escape behavior in the crayfish. Trends Neurosci 22, 153–161 (1999). [PubMed: 10203852]
22. Ryglewski S et al., Dendrites are dispensable for basic motoneuron function but essential for fine tuning of behavior. Proc Natl Acad Sci U S A 111, 18049–18054 (2014). PMC4273390. [PubMed: 25453076]
23. Gabitto MI et al., Bayesian sparse regression analysis documents the diversity of spinal inhibitory interneurons. Cell 165, 220–233 (2016). PMC4831714. [PubMed: 26949187]
24. Huang ZJ, Di Cristo G, Ango F, Development of GABA innervation in the cerebral and cerebellar cortices. Nat Rev Neurosci 8, 673–686 (2007). [PubMed: 17704810]
25. McBain CJ, Fisahn A, Interneurons unbound. Nat Rev Neurosci 2, 11–23 (2001). [PubMed: 11253355]
26. Bandler RC, Mayer C, Fishell G, Cortical interneuron specification: the juncture of genes, time and geometry. Curr Opin Neurobiol 42, 17–24 (2017). PMC5699457. [PubMed: 27889625]
27. Tripodi M, Arber S, Regulation of motor circuit assembly by spatial and temporal mechanisms. Curr Opin Neurobiol 22, 615–623 (2012). [PubMed: 22417941]
28. Gosgnach S et al., Delineating the diversity of spinal interneurons in locomotor circuits. J Neurosci 37, 10835–10841 (2017). PMC6596484. [PubMed: 29118212]
29. Li WC et al., Axon and dendrite geography predict the specificity of synaptic connections in a functioning spinal cord network. Neural Dev 2, 17 (2007). PMC2071915. [PubMed: 17845723]
30. Zipursky SL, Sanes JR, Chemoaffinity revisited: dscams, protocadherins, and neural circuit assembly. Cell 143, 343–353 (2010). [PubMed: 21029858]
31. Kwan KM et al., The Tol2kit: a multisite gateway-based construction kit for Tol2 transposon transgenesis constructs. Dev Dyn 236, 3088–3099 (2007). [PubMed: 17937395]
32. Livet J et al., Transgenic strategies for combinatorial expression of fluorescent proteins in the nervous system. Nature 450, 56–62 (2007). [PubMed: 17972876]

33. Zelenchuk TA, Bruses JL, In vivo labeling of zebrafish motor neurons using an mnx1 enhancer and Gal4/UAS. Genesis 49, 546–554 (2011). PMC3642388. [PubMed: 21538811]
34. Arrenberg AB, Del Bene F, Baier H, Optical control of zebrafish behavior with halorhodopsin. Proc Natl Acad Sci U S A 106, 17968–17973 (2009). PMC2764931. [PubMed: 19805086]
35. Kawakami K, Asakawa K, Muto A, Wada H, Tol2-mediated transgenesis, gene trapping, enhancer trapping, and Gal4-UAS system. Methods Cell Biol 135, 19–37 (2016). [PubMed: 27443919]
36. Higashijima S, Okamoto H, Ueno N, Hotta Y, Eguchi G, High-frequency generation of transgenic zebrafish which reliably express GFP in whole muscles or the whole body by using promoters of zebrafish origin. Dev Biol 192, 289–299 (1997). [PubMed: 9441668]
37. Satou C et al., Transgenic tools to characterize neuronal properties of discrete populations of zebrafish neurons. Development 140, 3927–3931 (2013). [PubMed: 23946442]
38. Bello-Rojas S, Istrate AE, Kishore S, McLean DL, Central and peripheral innervation patterns of defined axial motor units in larval zebrafish. J Comp Neurol 527, 2557–2572 (2019). PMC6688944. [PubMed: 30919953]
39. Koster RW, Fraser SE, Tracing transgene expression in living zebrafish embryos. Dev Biol 233, 329–346 (2001). [PubMed: 11336499]
40. Seredick SD, Van Ryswyk L, Hutchinson SA, Eisen JS, Zebrafish Mnx proteins specify one motoneuron subtype and suppress acquisition of interneuron characteristics. Neural Dev 7, 35 (2012). PMC3570319. [PubMed: 23122226]
41. Menelaou E, VanDunk C, McLean DL, Differences in the morphology of spinal V2a neurons reflect their recruitment order during swimming in larval zebrafish. J Comp Neurol 522, 1232–1248 (2014). PMC4692166. [PubMed: 24114934]
42. Meyer MP, Smith SJ, Evidence from in vivo imaging that synaptogenesis guides the growth and branching of axonal arbors by two distinct mechanisms. J Neurosci 26, 3604–3614 (2006). PMC6673851. [PubMed: 16571769]
43. Masino MA, Fetcho JR, Fictive swimming motor patterns in wild type and mutant larval zebrafish. J Neurophysiol 93, 3177–3188 (2005). [PubMed: 15673549]
44. Botev ZI, Grotowski JF, Kroese DP, Kernel density estimation via diffusion. Annals of Statistics 38, 2916–2957 (2010).
45. Bikoff JB et al., Spinal inhibitory interneuron diversity delineates variant motor microcircuits. Cell 165, 207–219 (2016). PMC4808435. [PubMed: 26949184]
46. Heitler WJ, Practical tools for analysing rhythmic neural activity. J Neurosci Methods 185, 151–164 (2009). [PubMed: 19765613]

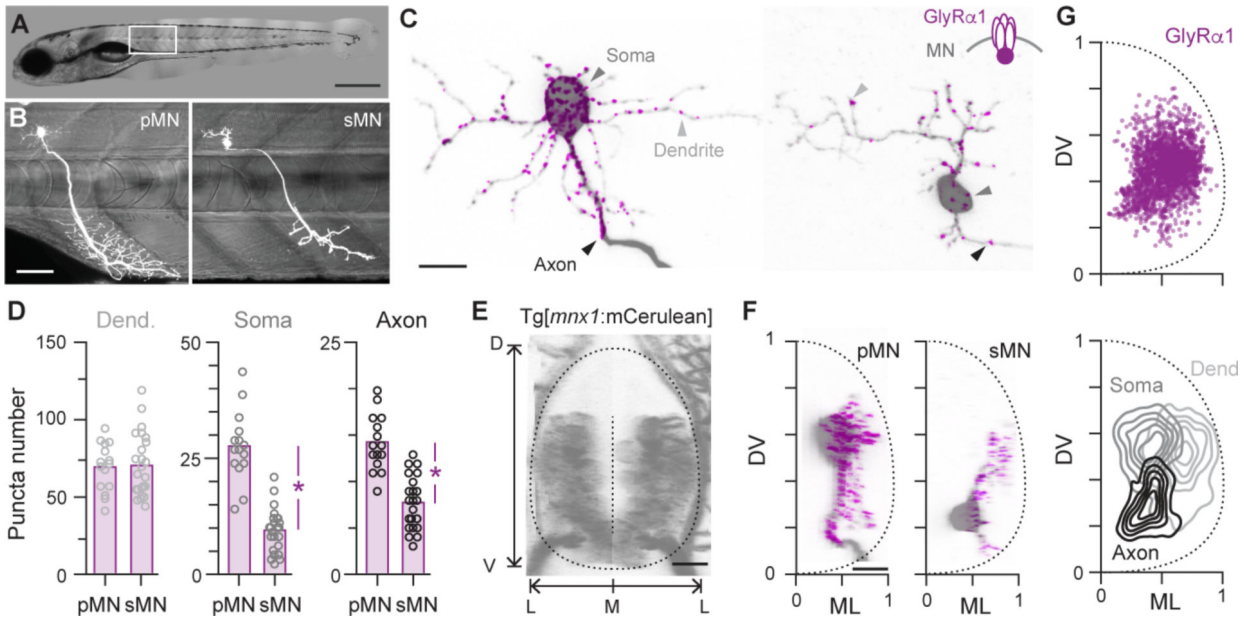

Fig 1. Differences in glycine synapse distribution related to motor neuron identity.

(A) Differential interference contrast image of a 5 day old larval zebrafish. Dorsal is up, rostral is left. Boxed region is illustrated in *B*. Scale bar, 0.5 mm.

(B) Sparse fluorescent labeling of a larger primary (pMN) and smaller secondary (sMN) motor neuron from different fish innervating axial muscle at midbody (see Methods). Scale bar, 50 μm.

(C) *Left*, confocal images of the pMN shown in *B* illustrates the distribution of GlyRα1-eGFP in different compartments. Scale bar, 10 μm. *Right*, distribution of GlyRα1-eGFP in the sMN shown in *B.*

(D) Quantification of GlyRα1-eGFP puncta in different compartments (Dend., dendritic; Soma, somatic; Axon, axonic) for primary and secondary motor neurons. Bars represent mean values. *, significant difference following two-tailed t-test. D, $t_{(37)} = 0.2$, $p = 0.81$; S, $t_{(37)} = 9.2$, $p < 0.05$; A, $t_{(37)} = 6.8$, $p < 0.05$; n = 15 pMNs and 24 sMNs.

(E), Confocal reconstruction in transverse view of the spinal cord of a Tg[*mnx1*:mCerulean] larva in which all motor neurons are labeled. The boundary of the spinal cord and midline used for anatomical landmarks is indicated by dashed lines. D, dorsal; V, ventral; M, medial; L, lateral. Scale bar, 10 μm.

(F), Transverse views of confocal images provided in *c* registered to dorsoventral (DV) and mediolateral (ML) landmarks. Scale bar, 10 μm.

(G), *Top*, Quantification of the distribution of GlyRα1-eGFP puncta normalized to DV and ML landmarks. n = 39 neurons and 3100 putative synapses. *Bottom*, contour density plots of the DV and ML distribution of dendritic (Dend.), somatic (Soma) and axonic (Axon) contacts (see Methods).

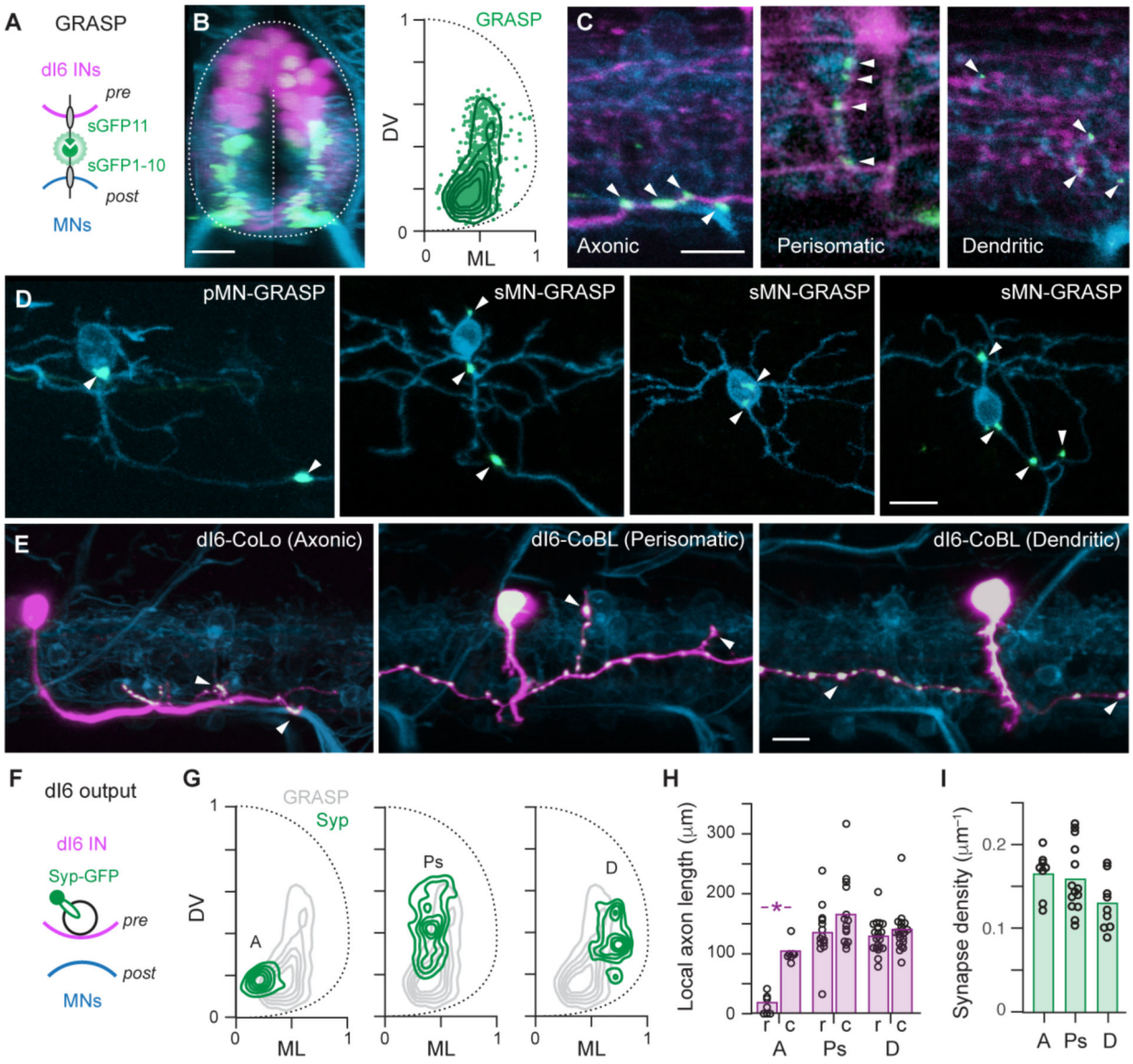

Fig 2. Different motor neuron compartments are targeted by different dI6 neurons.

(A) Schematic illustrating co-expression of pTagRFP (pink) and one half of the split GFP molecule (sGFP11, green) in presynaptic (pre) dI6 neurons and mCerulean (blue) and the other half of the split GFP molecule (sGFP1–10, green) in postsynaptic (post) motor neurons. Split GFP constructs are targeted to the membrane using CD4 (black).

(B) *Left*, transverse view of compound transgenic line labeling all dI6 neurons (pink), all motor neurons (blue) and the resulting GRASP signal (green). The boundary of the spinal cord and midline used for anatomical landmarks is indicated by dashed lines. Scale bar, 10 μm. *Right*, distribution of GRASP puncta (green data points; n = 15 fish, 908 GRASP puncta) and a contour density plot (green lines) normalized to dorsoventral (DV) and mediolateral (ML) landmarks.

(C) Single optical sections of confocal images from a lateral view. White arrowheads indicate axonic (left), perisomatic (middle) and dendritic (right) GRASP signals. Scale bar, 10 μm.

(D) Lateral views of GRASP labeling in individual primary (pMN) and secondary (sMN) motor neurons (white arrowheads). Motor neurons are sparsely labeled by mCerulean and sGFP1–10, while dI6 neurons are sparsely labeled by sGFP11. Scale bar, 10 μm.
(E) Lateral views of dI6 neurons sparsely labeled with cytosolic pTagRFP (pink) and synaptophysin-GFP (green, white indicates co-localization) in the Tg[*mnx1*:mCerulean] motor neuron line (blue). White arrowheads indicate likely axonic (left), perisomatic (middle) and dendritic (right) connections. Scale bar, 10 μm.
(F) Schematic illustrating the procedure for co-expressing pTagRFP (pink) and synaptophysin-GFP (green) in presynaptic (pre) dI6 neurons and mCerulean (blue) in postsynaptic (post) motor neurons to assess dI6 output.
(G) Contour density plots of the distribution of synaptophysin puncta for axonic (A, left), perisomatic (Ps, middle) and dendritic (D, left) dI6 neurons. Axonic (n = 5), Perisomatic (n = 4), Dendritic (n = 6).
(H) Quantification of local commissural axon length measured 100 micrometers rostral (r) and caudal (c) to the soma for the distinct types of dI6 neurons. Bars represent mean values. *, significant difference following Mann-Whitney U tests. Axonic, $U_{(12)} = 0$, $p < 0.05$, n = 7; Perisomatic, $U_{(26)} = 70$, $p = 0.54$, n = 14; Dendritic, $U_{(40)} = 186$, $p = 0.79$, n = 21.
(I) Quantification of synapse density for the distinct types of dI6 neurons. Bars represent mean values. Densities are not significantly different following one-way ANOVA ($F_{(2,28)} = 2.76$, $p = 0.08$). Axonic (n = 8), perisomatic (n = 14), dendritic (n = 9).

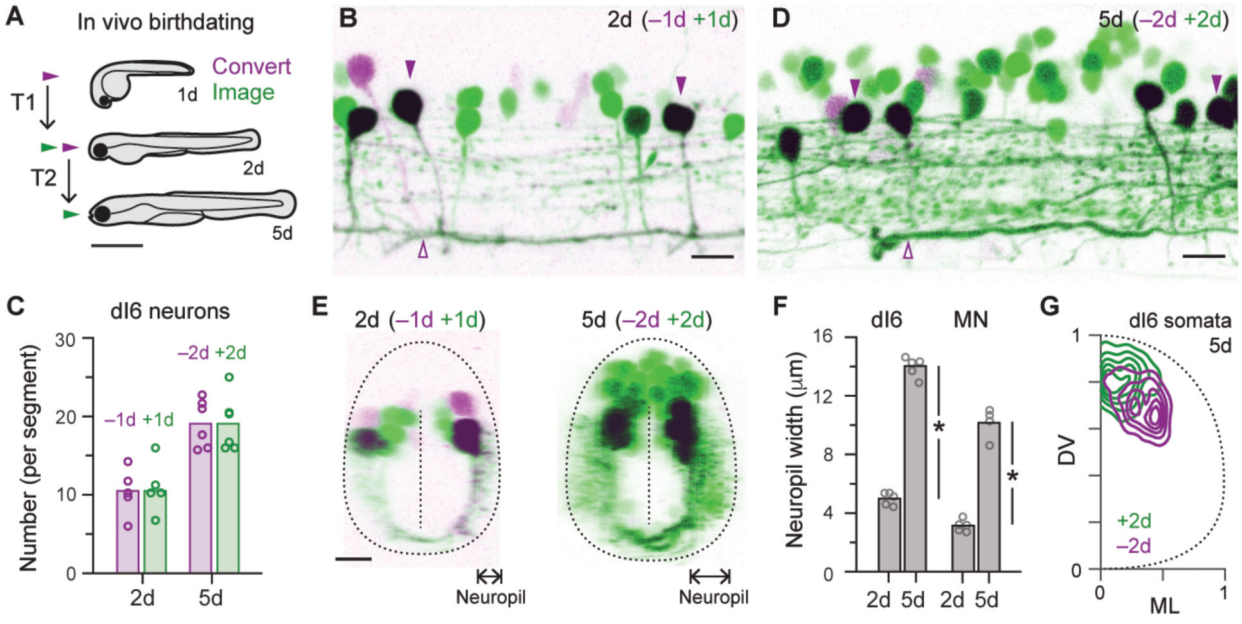

Fig 3. dI6 neurons emerge in a developmental sequence like motor neurons

(A) Schematic illustrating the procedure for using staged photoconversions to birthdate neurons in vivo. For the first time period (T1), photoconversions are performed in 1 day old embryos (1d) and imaged on day 2. For second time period, photoconversions are performed in 2 day old embryos and imaged on day 5 (5d). Scale bar, 1 mm.

(B) Lateral view of single spinal segment in 2 day old Tg[*dmrt3a*:Gal4; UAS:Dendra] embryo (2d). dI6 neurons that had differentiated on or before day 1 (−1d) are purple/black, while those that differentiated after day 1 (+1d) are green. Purple arrowheads mark dI6-CoLo neurons, which are distinguishable based on their large caliber axons. Scale bar, 10 μm.

(C) Quantification of the number of old (purple) and new (green) neurons per segment on day 2 (2d) and day 5 (5d) based on staged photoconversions. Data points are from different fish and bars represent mean values.

(D) Lateral view of single spinal segment in 5 day old Tg[*dmrt3a*:Gal4; UAS:Dendra] larva (5d). dI6 neurons that had differentiated on or before day 2 (−2d) are purple/black, while those that differentiated after day 2 (+2d) are green. Scale bar, 10 μm.

(E) *Left*, transverse view of 2 day old Tg[*dmrt3a*:Gal4; UAS:Dendra] embryo illustrated in *B*. *Right*, transverse view of 5 day old Tg[*dmrt3a*:Gal4; UAS:Dendra] larvae illustrated in *D*. Neuropil width measures indicated by arrows.

(F) Quantification of the width of the neuropil on day 2 (2d) and 5 (5d) for dI6 neurons and motor neurons (MN). Bars represent mean values. *, significant difference following two-tailed t-test. dI6 neurons, $t_{(8)} = 24.7$, $p < 0.05$, n = 5 (2d and 5d); MNs, $t_{(7)} = 13.7$, $p < 0.05$, n = 5 (2d) and n = 4 (5d).

(G) Contour density plot of the distribution of dI6 neuron somata on day 5 (5d) that were born on or before (purple) or after (green) day 2. n = 5 larvae, 173 neurons (<2d) and 173 neurons (>2d) measured over ~4 consecutive hemi-segments.

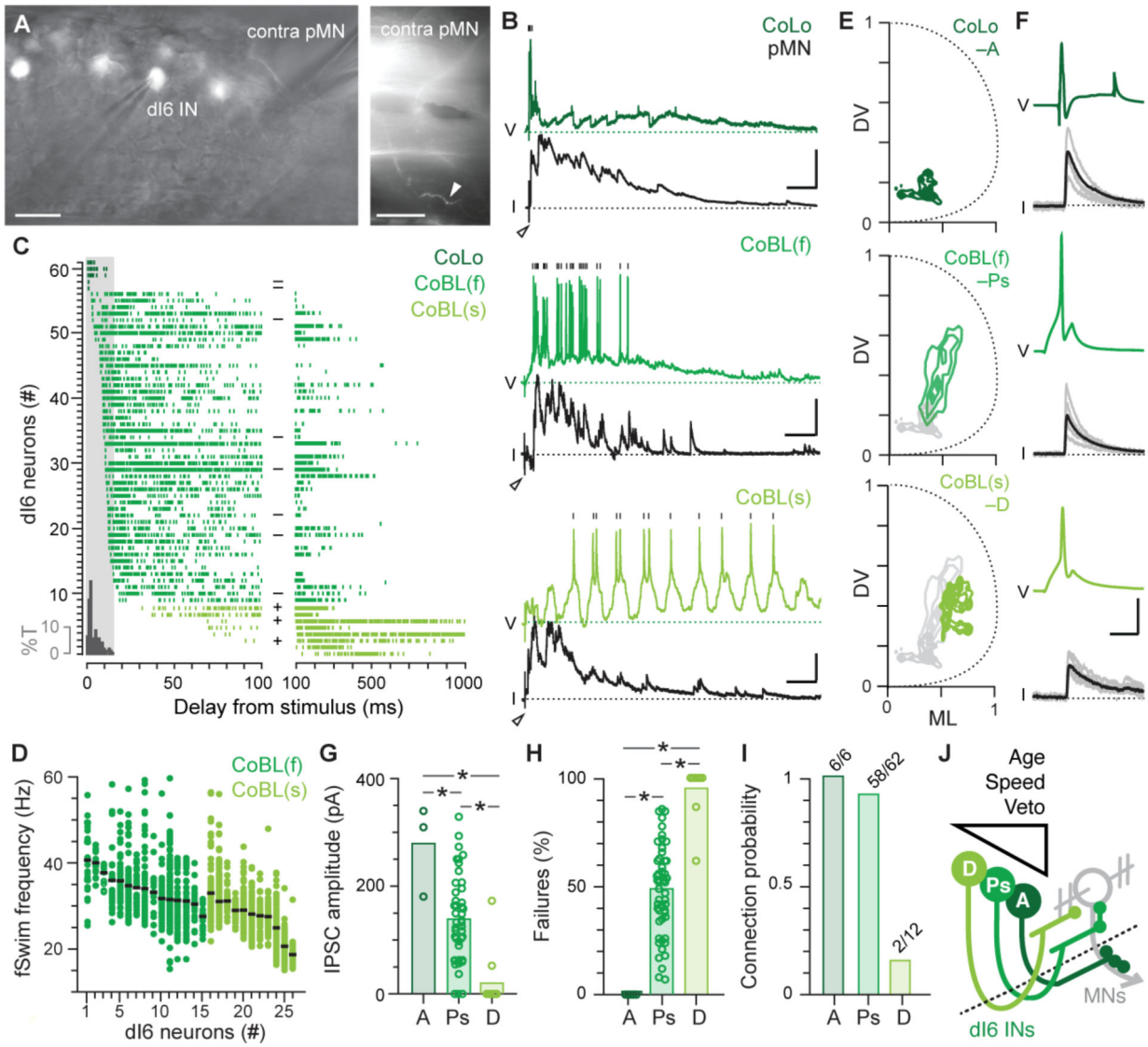

Fig 4. dI6 morphology and birth order match recruitment order and inhibitory strength

(A) *Left*, lateral view of single spinal segment in a Tg[*dmrt3a*:hsGFP] larva illustrates patch-clamp electrodes targeting a dI6 interneuron (IN) and a primary motor neuron (pMN) on the contralateral side (contra). Scale bar, 10 μm. *Right*, lateral, lower magnification view of single muscle segment illustrating the peripheral axon of the contralateral pMN (white arrowhead) captured after recording. Scale bar, 50 μm.

(B) Paired patch-clamp recordings between dI6 neurons and primary motor neurons (pMN) are arranged from top to bottom based on recruitment patterns following the tail stimulus (at open arrowheads). Vertical black lines mark spikes in the dI6 neuron recorded in current-clamp. Voltage-clamp recordings from pMNs held at 0 mV (black dashed line) reveal outward IPSCs. V, voltage; I, current. Scale bars, dI6-CoLo, 10 mV, 800 pA, 50 ms; faster dI6-CoBL (f), 20 mV, 200 pA, 50 ms; slower dI6-CoBL (s), 10 mV, 200 pA, 50 ms.

(C) Spike raster plots normalized to the tail stimulus (time = 0) are arranged from top to bottom based on latency and color-coded according to recruitment pattern during fictive

swimming illustrated in *B* (CoLos, #57–61; faster CoBLs, #9–56; slower CoBLs, #1–8). Each row represents spiking in multiple fictive swim episodes from the same dI6 neuron. The onset of short-latency inhibitory post-synaptic currents (IPSCs) to motor neurons on the contralateral side is illustrated in the grey histogram and expressed as percentage of total IPSCs (%T). dI6 neurons present on or before (−) and after (+) day 2 based on staged photoconversions are noted in the middle of the plot. Note the differences in timescale between the left and right sides of the plot.

(D) Quantification of the range of fictive swimming (fSwim) frequencies in a subset of recordings (n = 26 out of 61) at which faster (f) and slower (s) dI6-CoBL neurons are recruited, arranged from left to right based on mean frequency (black lines).

(E) Contour density plots of the distribution of axon terminals for axonic CoLos (A, top), faster perisomatic CoBLs (Ps, middle) and slower dendritic CoBLs (D, bottom). Axonic (n = 2), Perisomatic (n = 4), Dendritic (n = 5).

(F) Current evoked spikes in dI6 neurons (green) and IPSCs in primary motor neurons (black) from a dI6-CoLo (top), faster dI6 CoBL (middle) and slower dI6 CoBL (bottom). Solid lines are averages while grey lines represent individual sweeps. Current steps (not shown) are 5 ms in duration for the CoBLs and 10 ms for the CoLo. Scale bar, 20 mV, 200 pA, 5 ms.

(G) Quantification of mean IPSC amplitude for axonic (A), perisomatic (Ps) and dendritic (D) dI6 neurons. Bars represent mean values. *, significant difference using Kruskal-Wallis ANOVA ($H_{(2)} = 23.9$, $p < 0.05$, n = 66) followed by Mann-Whitney U-tests with Bonferroni corrections. A (n = 3) – Ps (n = 51), $U_{(52)} = 138$, $p < 0.05$; A (n = 3) – D (n = 12), $U_{(13)} = 36$, $p < 0.05$; Ps (n = 51) – D (n = 12), $U_{(61)} = 56$, $p < 0.05$). Note, only 3/6 axonic dI6 recordings could be included for analysis based on series resistance criteria.

(H) Quantification of failure rate for axonic (A), perisomatic (Ps) and dendritic (D) dI6 neurons. Bars represent mean values. *, significant difference using Kruskal-Wallis ANOVA ($H_{(2)} = 35.6$, $p < 0.05$, n = 74) followed by Mann-Whitney U-tests with Bonferroni corrections. A (n = 6) – Ps 25 (n = 56), $U_{(60)} = 0$, $p < 0.05$; A (n = 6) – D (n = 12), $U_{(16)} = 0$, $p < 0.05$; Ps (n = 56) – D (n = 12), $U_{(66)} = 633$, $p < 0.05$).

(I) Quantification of probability of forming a connection with a primary motor neuron for axonic (A), perisomatic (Ps) and dendritic (D) dI6 neurons. Numbers noted above each bar.

(J) Schematic summarizing the results. Dashed line is the midline. See text for details.